Journal of Materials Chemistry C

The effect of halogen on the structural, optoelectronic, and luminescent properties of hybrid (1,5-Pentanediamine)PbX_4 (X=Cl, Br, I) perovskites

Journal:	*Journal of Materials Chemistry C*
Manuscript ID	TC-ART-08-2023-002767.R2
Article Type:	Paper
Date Submitted by the Author:	20-Nov-2023
Complete List of Authors:	Shtarev, Dmitry; Institute of Tectonics and Geophysics Named After U A Kosygin FEB RAS, Balanov, Mikhail; Institute of High Technologies and Advanced Materials of the Far Eastern Federal University Mayor, Aleksandr; IACP FEB RAS Gerasimenko, Andrey; Institute of Chemistry FEB RAS Kevorkyants, Ruslan; St. Petersburg State University, Photonics Zharovov, Dmitrii; St Petersburg State University, Photonics Bulanin, Kirill; Saint-Petersburg State University, Physics Pankin, Dmitry; Sankt-peterburgskij gosudarstvennyj universitet Rudakova, Aida; Sankt-peterburgskij gosudarstvennyj universitet, Laboratory of Photoactive Nanocomposite materials Chaplygina, Darya; Far Eastern Federal University Selivanov, Nikita; St. Petersburg State University, Photonics Emeline, Alexei; St-Petersburg State University

The effect of halogen on the structural, optoelectronic, and luminescent properties of hybrid (1,5-Pentanediamine)PbX_4 (X=Cl, Br, I) perovskites

D.S. Shtarev[1,2a,*], M.I. Balanov[1,2,b], A.Ju. Major[2,3,c], A.V. Gerasimenko[4,d], R. Kevorkyants[5,e], D.A. Zharovov[5,f], K.M. Bulanin[6,g], D.V. Pankin[6,7,h], A.V. Rudakova[6.i], D.A. Chaplygina[2,j], N.I. Selivanov[5,k], A.V. Emeline[5,l]

[1] Department of Materials Science, Shenzhen MSU-BIT University, PRC.
[2] Institute of High Technologies and Advanced Materials of the Far Eastern Federal University, Vladivostok, Russky Island, Ajax, 10, 690022, Russian Federation.
[3] Institute of Automation and Control Processes, Far Eastern Branch, Russian Academy of Sciences, Russian Federation.
[4] Institute of Chemistry, Far Eastern Branch, Russian Academy of Sciences, Russian Federation.
[5] Saint-Petersburg State University, Laboratory 'Photoactive Nanocomposite Materials', Russian Federation.
[6] Saint-Petersburg State University, Laboratory 'Photonics of Crystals', Russian Federation.
[7] Saint-Petersburg State University, Center for Optical and Laser Materials Research, Russian Federation.

[a] shtarev@mail.ru, [b] balanov.mi@dvfu.ru, [c] mayor@iacp.dvo.ru, [d] gerasimenko@ich.dvo.ru, [e] ruslan.kevorkyants@gmail.com, [f] dmzharovov@gmail.com, [g] k.bulanin@spbu.ru, [h] dmitrii.pankin@spbu.ru, [i] aida.rudakova@spbu.ru, [j] chaplygina.dal@dvfu.ru, [k] selivanov_chem@mail.ru, [l] alexei.emeline@spbu.ru

* - Corresponding author (ORCID: 0000-0002-1274-0183)

Abstract

The present work reports on experimental structures, optoelectronic, and luminescence properties of the series of low-dimensional hybrid organic-inorganic (1,5-Pentanediamine)PbX_4 (X=Cl, Br, I) perovskites. Single-crystal XRD data revealed that the chloride and bromide compounds form quasi 2D perovskite-like structures, whereas the iodide is quasi 1D compound. In accordance with experiment, DFT modeling predicts that the chloride and bromide are direct bandgap semiconductors. In contrast, the iodide is an indirect bandgap semiconductor. Experimentally and theoretically established bandgaps widths of the perovskites follow the same trend. Finally, luminescent properties of the perovskites were investigated. The study shows that the halogen anions determine the degree of disorder of the perovskite crystal lattices and degree of distortion of PbX_6 octahedra therein. Both structural phenomena affect dimensionality, optoelectronic, and luminescent properties of the studied perovskites.

Keywords: Low-dimensional perovskites, HOIPs, Luminescence, DFT

1. Introduction

Nowadays, hybrid organic-inorganic perovskites or perovskite-like structures (Ruddlesden-Popper, Dion-Jacobson phases) are among the most promising light-transforming materials. Mainly, they are intended to be used in solar panels for a direct transformation of solar radiation into electric current [1] or in light-emitting diodes (LEDs) for white light sources, narrow-band light of a specific color, and even for laser generation [2-6]. Whereas hybrid 3D perovskites are best suited for photovoltaics, low-dimensional quasi 1D and 2D perovskites pave the way to various light-emitting applications.

In hybrid quasi 2D halide perovskites the layers of inorganic octahedra MX_6 are separated from each other by the layers of organic cations. The latter often represent diamines. Two amino groups of such cation form hydrogen bonds with neighboring layers of inorganic MX_6 octahedra. This choice of organic cation is intended to increase the stability of perovskite crystal [7]. The number of organic cations used to form quasi 2D perovskite structures is ever-increasing. At present, several hundreds of them are already known [8].

A particular sub-family of low-dimensional hybrid halide perovskites contain alkanediamine cations with terminal amino-groups, i.e. NH_3-$(CH_2)_n$-NH_3. In contrast to hybrid halide perovskites with aromatic organic cations demonstrating strong interaction of inorganic electronic subsystem with an organic one, members of this sub-family feature only hydrogen bonding interaction between inorganic and organic subsystems. Their alkyl chain lengths are directly related to the distance between the layers of inorganic MX_6 octahedra. However, their electronic and optical properties are not directly affected by the length of alkyl chain being governed solely by the inorganic subsystem composition as we have showed recently using 1,6-hexamethylenediaminium perovskite as an example [9].

As a rule, quasi 2D hybrid perovskites show complex luminescence properties [10] combining narrow-band and broadband luminescence. The narrow-band luminescence is usually attributed to the luminescence of free excitons [11]. While still debated, the nature of broadband luminescence is attributed to both the luminescence of autolocalized excitons [11] and to the luminescence at crystal lattice defects [12].

Generally, luminescence properties of hybrid low-dimensional perovskites are considered through the prism of the structure of their organic cation (linear [13], branched or cyclic, presence or absence of double bonds, etc. [11]). Much less attention is paid to the structural role of halogen.

Here, we focus on haloplumbates with 1,5-pentamethylenediaminium (PDA) cation. It was known that the use of PDA as a cation in the synthesis of hybrid lead iodide perovskite leads to a formation of low-dimensional (quasi 1D) crystals in which chains of the inorganic PbI_6 octahedra are oriented along [111] crystallographic direction [14]. This was the only scarce piece of information one could find in the literature until very recently. A more detailed information about the crystal structure, electronic, and optical properties of $PDAPbCl_4$ was reported not that long ago [15]. Here, a comparative study of the effect of halogen on the dimensionality, structure, optoelectronic, vibrational, and luminescence properties of $PDAPbX_4$ (X = Cl, Br, I) perovskites is conducted.

2. Experimental and modeling techniques

2.1. Synthesis

The samples of $PDAPbX_4$ (X=Cl, Br, I) were prepared using 'wet-chemistry' approach.

Materials: Lead (II) bromide ($PbBr_2$, 98%, Acros Organics), lead (II) iodide (PbI_2, 99%, Acros Organics), lead (II) chloride ($PbCl_2$, 99%, Acros Organics), hydroiodic acid (HI, 56% in water, Iodobrom), hydrobromic acid (HBr, 40% in water, Iodobrom), hydrochloric acid (HCl, 36% in water, NevaReaktiv), 1,5-diaminopentane (PDA) ($C_5H_{14}N_2$, 98%, Macklin) were purchased and used in this work. All reagents were used as received without further purification.

Synthesis of $C_5H_{16}N_2PbCl_4$ ($PDAPbCl_4$): $PbCl_2$ (2.00 g; 7.19 mmol) and PDA (0.73 g; 7.19 mmol) were separately dissolved in 47 ml and 9 ml of HCl, respectively. Then, the resulting solutions were mixed, and crystalline precipitate was formed after several days. The obtained crystals were filtered, washed with HCl, and thereafter with acetone. Finally, the crystals were dried in a vacuum oven at 50°C.

Synthesis of $C_5H_{16}N_2PbBr_4$ ($PDAPbBr_4$): $PbBr_2$ (2.00 g; 5.45 mmol) and PDA (0.56 g; 5.45 mmol) were separately dissolved in 9 ml of HBr. Then, the resulting solutions were mixed, and

crystalline precipitate was formed after a few minutes. The reaction mixture was heated until complete dissolution of the precipitate and then cooled slowly to room temperature. The obtained crystals were filtered, washed with HBr, and thereafter with acetone. Finally, the crystals were dried in a vacuum oven at 50°C.

Synthesis of $C_5H_{16}N_2PbI_4$ ($PDAPbI_4$): PbI_2 (2.00 g; 4.34 mmol) and PDA (0.44 g; 4.34 mmol) were separately dissolved in 9 ml of HI. Then, the resulting solutions were mixed, and crystalline precipitate was formed after a few minutes. The reaction mixture was heated until complete dissolution of the precipitate and then cooled slowly to room temperature. The obtained crystals were filtered, washed with HI, and thereafter with acetone. Finally, the crystals were dried in a vacuum oven at 50°C.

2.2. Characterization

The powder diffraction data of $PDAPbX_4$ (X=Cl, Br, I) was collected at room temperature with a Colibri powder diffractometer (Bourevestnik, Cu-Kα radiation) and linear VANTEC detector. The step size of 2θ was 0.02° and the counting time was 35.4 s per step.

The full profile X-ray analysis of $PDAPbBr_4$ and $PDAPbCl_4$ single-crystals was performed using Bruker Kappa Apex II diffractometer with graphite-monochromatized MoK_α radiation [16] at 100 K. The data reduction and multi-scan absorption correction was carried out using original software.

Diffuse reflectance spectra were recorded in the spectral range [200-800] nm under ambient conditions using Lambda 950 UV/vis/NIR spectrophotometer. An optical-grade $BaSO_4$ powder was used as a reference standard.

The Raman spectra of samples ($PDAPbBr_4$ and $PDAPbI_4$ single crystals and $PDAPbCl_4$ powder) were obtained using Senterra (Bruker) Raman spectrometer equipped with Olympus BX51 microscope in backscattering geometry. The Raman scattering was excited with 785 nm solid state laser. The laser power under the 20x lens with 14 μm spot diameter was ~1 mW. The diffraction grating was 400 l/mm, the aperture was 25x1000 μm. The accumulation time was 150 s with 6 repetitions.

FTIR spectra of the powdered samples were obtained using at Nicolet 8700 (Thermo Scientific) FTIR spectrometer with ATR diamond accessory. The KBr beamsplitter and the liquid nitrogen cooled

mercury-cadmium-telluride type (MCT-A) detector were used. The spectra were obtained with 4 cm^{-1} resolution and Blackman-Harris apodization function. 150 scans were accumulated of each spectrum. The phase correction was performed according to the Mertz method.

Low-temperature luminescence spectra and luminescence excitation spectra of the perovskite samples in the spectral range [250–850] nm were registered using the spectrofluorometer Jobin-Yvon FluoroMax Plus. All the recordings were performed using the modified sample holder enabling a precise setup at every spectrum registration stage. The radiation within particular spectral ranges was filtered with glass color filters. Prior to the spectra recordings, the vacuumized samples were placed in the optical nitrogen cooled cryostat LN-121-SPECTR (Cryotrade engineering, Russia) compatible with the spectrofluorometer Jobin-Yvon FluoroMax Plus. The cryostat windows are made from high quality quartz КУ-1 transparent in all the studied spectral regions. The temperature control was accomplished via the integrated thermocouple and thermoregulation unit TPM-210. The luminescence lifetimes were determined using a setup described in detail in the supplementary materials.

2.3. Computational approach

Electronic structures of $PDAPbX_4$ perovskites were modeled theoretically using a periodic DFT approach. This was accomplished by employing the Plane Augmented Wave (PAW) approach [17] in conjunction with the Generalized Gradient Approximation (GGA) Perdew-Burke-Ernzerhof (PBE) [18,19] density functional as implemented in VASP 5.4.4 program [20-23]. The $P2_1/c$ spatial symmetry of the perovskite crystal lattices determined by XRD was employed. The perovskite unit cells correspond to the chemical formula $Pb_4X_{16}C_{20}N_8H_{64}$ (X=Br, I). The chloride unit cell is twice as large. The reason for this is given later in the text. SCF energy convergence criterion was set to $1.0x10^{-7}$ eV. Atomic kinetic energy cutoffs were set to their default values. Brillouin Zones (BZ) were sampled over the Monkhorst–Pack grid [24] of 7x9x9 k-points (9x9x3 k-points for the monocrystalline chloride perovskite). Electronic band structures were computed at 181 k-points along the high symmetry path Γ-A-C-D-D1-E-X-Y-Y1-Z of monoclinic BZ. Electronic band structures and density of states were

plotted using the Gnuplot 5.2 software package [25]. Throughout the text, chemical structures are visualized using the program VESTA [26].

For $PDAPbI_4$ perovskite, the calculations of phonon properties at Γ-point were carried out in the framework of GGA PBE density functional and norm-conserving pseudopotentials as implemented in the CASTEP software (Materials Studio) [27,28]. The plane wave basis cutoff energy was set to 1000 eV. The SCF energy convergence criterion was set to $5x10^{-7}$ eV. Dimension of *k*-space was chosen in order to provide a step of 0.05 1/Å in *k*-space. The Monkhorst–Pack grid was chosen. At the initial stage, the geometry optimization was carried out with the aid of the Limited-memory Broyden–Fletcher–Goldfarb–Shanno (LBFGS) method [29] to achieve residual forces and stresses below 0.01 eV/Å and 0.02 GPa, respectively. For the optimized structure, the phonon frequencies were calculated by the linear response method (Density Functional Perturbation Theory) [30].

3. Results

3.1. Crystal structure of the $PDAPbX_4$ perovskites

Powder XRD patterns of the three hybrid perovskites are shown in Figure S1. The reference XRD data available only for $PDAPbI_4$ [14]. The XRD pattern of $PDAPbI_4$ matches well the reference XRD pattern indicating the formation of the perovskite. XRD patterns of the chloride and bromide compounds significantly differ from that of the iodide sample. The single main reflection at ~8° in both XRD patters corresponds to the interplane distances of 11.25 Å and 10.12 Å for the chloride and bromide perovskite, respectively. This observation suggests quasi 2D structure for the chloride and bromide species.

The structures of $PDAPbCl_4$ and $PDAPbBr_4$ perovskites were investigated using single crystal XRD technique as well. The resolved non-hydrogen atomic positions were refined by the least-squares method in anisotropic approximation. All the hydrogen atoms were placed in geometrically idealized positions which were then refined using the riding-model approximation with r(C-H) = 0.99 Å, r(N-H) = 0.91 Å, and Uiso(H) = 1.2 or 1.5 times Ueq(C, N). The determination and refinement of the structures were carried out using the SHELXTL program [31]. Some details of the data collection,

processing, and refinement are given in Table S1. Further details can be obtained from the Cambridge Crystallographic Data Center by quoting the depository number CCDC – 2269541 (for $NH_3(CH_2)_5NH_3PbCl_4$) and CCDC – 2269539 (for $NH_3(CH_2)_5NH_3PbBr_4$).

Resolved structures of the chloride and bromide perovskites as well as the known structure of the iodide are illustrated in Figure 1. Both the chloride and bromide species demonstrate quasi 2D perovskite-like structure in which corner-sharing inorganic octahedra form 2D sheets separated from each other by organic cations. Based on the single crystal XRD patterns of the chloride and bromide perovskite their powder XRD patterns were simulated. Both of them are demonstrated in Figure S1 as well. It shows a good match between the experimental and calculated data.

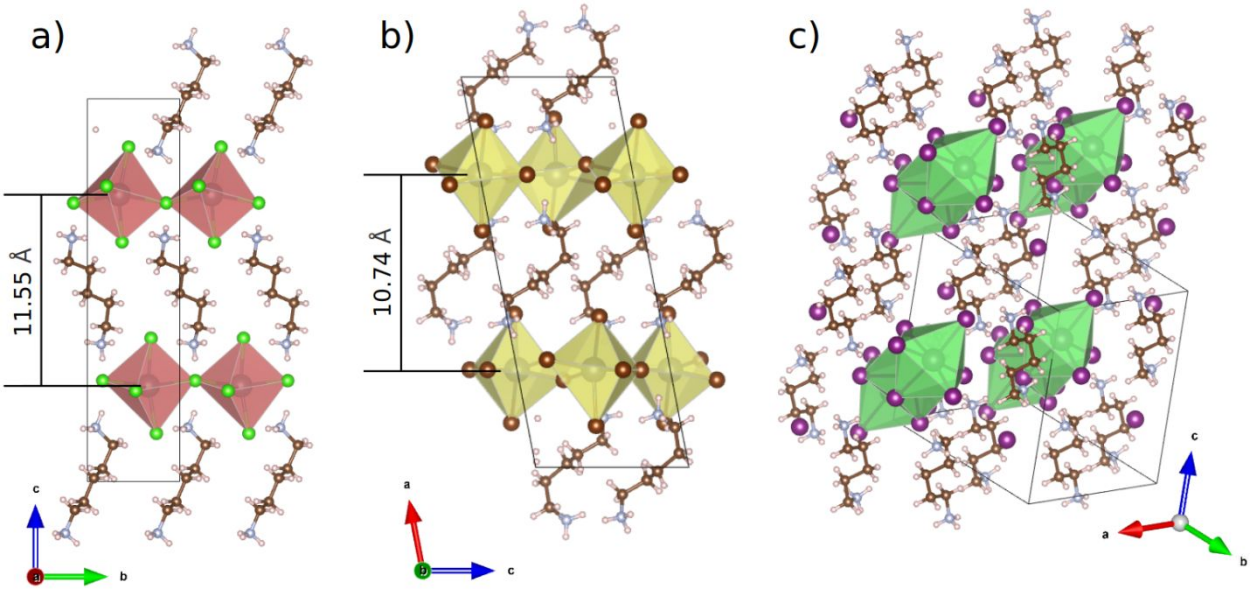

Figure 1. Single crystal XRD structures of a) $PDAPbCl_4$, b) $PDAPbBr_4$ and literature data for c) $PDAPbI_4$.

The obtained structural data enables analysis of the sizes of inorganic octahedra PbX_6 and the degrees of their disorder and distortion as a function of halogen type (see Table 1). Average Pb-X distances (d_{av}), the degree of PbX_6 octahedra distortion (Δd) as well as the octahedral angle variance σ_{oct}^2 were calculated according to the following formulae [32]:

$$d_{av} = \frac{1}{12}\sum_{i=1}^{i=12} d_i, \quad (1)$$

$$\Delta d = \frac{1}{12}\sum_{i=1}^{i=12}\frac{(d_i - d_{av})^2}{d_i}, \quad (2)$$

$$\sigma_{oct}^2 = \frac{1}{12}\sum_{i=1}^{i=12}(\alpha_i - 90)^2, \quad (3)$$

where d_i – length of the bond i (i=12) and α_i – angle X-Pb-X. The averaging is done over two octahedra of the perovskite primitive cells.

The value d_{av} serves as a measure of an average size of the PbX_6 octahedra. Table 1 shows that in the sequence Cl-Br-I the octahedra sizes increase. This dependence takes place due to two effects. First, the halogen anion sizes increase in the same sequence. Second, electronegativity of the halogen anions decrease in that sequence.

The perovskite octahedra appear to be distorted that is manifested by a dispersion in the Pb-X bond lengths (eq. 2) and/or by a displacement of lead cations away from the octahedra centers (eq. 3). As can be seen from Table 1, the dispersion in Pb-Cl bond lengths is about an order of magnitude smaller than that in Pb-Br bond lengths. In this respect, the PbI_6 octahedra are the most distorted. At the same time, the $PbCl_6$ octahedra feature the largest displacement of lead cations from centers of the octahedra. In the case of $PbBr_6$ and PbI_6 octahedra this displacement is an order of magnitude smaller.

Yet another type of a perovskite inorganic subsystem structural phenomenon is a tilt of the octahedra PbX_6 with respect to each other. Usually, it is characterized by an angle Pb-X-Pb (denoted as Θ_{av} in Table 1) [33]. The more it deviates from 180 ^{0} (angle Pb-X-Pb in ideal 3D perovskites) the stronger is the perovskite crystal lattice disorder. Table 1 shows that PbX_6 octahedra tilting in the chloride perovskite (Θ_{av}=145.83°) is just slightly stronger than in the bromide one (Θ_{av}=150.53°). Both tilting angles, however, deviate insignificantly from the ideal angle of 180° enabling the formation of quasi 2D perovskite structure. In contrast, in the iodide perovskite, the PbI_6 octahedra tilting is very large (Θ_{av}=75.19°). This results in the edge- and face-sharing PbI_6 octahedra leading to a quasi 1D perovskite structure.

Table 1. Structural features of the PbX_6 octahedra: Average Pb-X distance d_{av} and distortion Δd, Å; average X-Pb-X angle variance σ_{oct}^2 and Pb-X-Pb angle Θ_{av}, degrees.

Compound	Pb-X, Å	Δd, Å	X-Pb-X σ^2_{oct}	Pb-X-Pb Θ_{av}
$PDAPbCl_4$	2.8624	$5.45*10^{-5}$	231.62	145.83
$PDAPbBr_4$	2.9916	$3.48*10^{-4}$	20.37	150.53
$PDAPbI_4$	3.2260	$1.12*10^{-3}$	28.89	75.19

Also, for all the perovskites, the distances from nitrogen atom to the nearest halogen atoms were determined. For the iodide specie, the $-NH_3^+$ groups are arranged between the zigzag-like chains of the PbI_6 octahedra. Distances from the $-NH_3^+$ groups to the nearest three iodine atoms appear to be 3.53 Å, 3.67 Å, and 3.98 Å. In the chloride perovskite, the $-NH_3^+$ groups are located in cavities formed by four $PbCl_6$ octahedra which share corners so that there are three nearest chlorine atoms, and the N···Cl distance varies within 0.2 Å: 3.21 Å, 3.28 Å, and 3.38 Å. As mentioned above, in the bromide perovskite, two sets of $-NH_3^+$ groups insignificantly differing in distance from nitrogen atom to three nearest bromine atoms were found. The distances r(N···Br) for the first set: 2.94 Å, 3.35 Å, 3.41 Å, while for the second one: 3.09 Å, 3.34 Å, 3.46 Å. $PbBr_6$ octahedra in $PDAPbBr_4$ perovskite are arranged in a way similar to that of $PbCl_4$ octahedra in the corresponding specie. Thus, distances from the $-NH_3^+$ groups to the bromine atoms allow the formation of weak hydrogen bonds N-H···X.

Figure 1 also shows distances between the planes formed by lead atoms in the quasi 2D perovskites $PDAPbCl_4$ (11.55 Å) and $PDAPbBr_4$, (10.74 Å). These values derived from the single crystal XRD data are very close to their counterparts obtained from the analysis of the powder X-ray diffraction patterns: 11.25 Å ($PDAPbCl_4$) and 10.12 Å ($PDAPbBr_4$). Presumably, such differences in interplane distances between the chloride and bromide compounds cannot be related to the sizes of inorganic octahedra alone. Here, the organic cation orientation could play an important role as well. Indeed, Figure 1 shows that in the chloride perovskite the organic cation is oriented almost perpendicular to the planes formed by the lead atoms, whereas in the bromide perovskite the organic cation is inclined to them at the angle of ~45.0°.

3.2 Vibrational spectroscopic studies

FTIR and Raman spectra of $PDAPbX_4$ samples were recorded at room temperature in the spectral regions [700–4000] cm^{-1} and [70–4000] cm^{-1}, respectively (see Figures S2 and S3). The majority of observed bands are interpreted in Table S2. The computed vibrational modes of $PDAPbI_4$ active in IR absorption spectrum are given there as well. The calculated and experimental data show very good agreement and help to identify vibrational modes for $PDAPbCl_4$ and $PDAPbBr_4$ (Figure S2). The Raman spectra low-frequency region in Figure 2 is due to lattice vibrations involving heavy Pb and X atoms. The PDA cations are inactive in this spectral region and behave as rigid species.

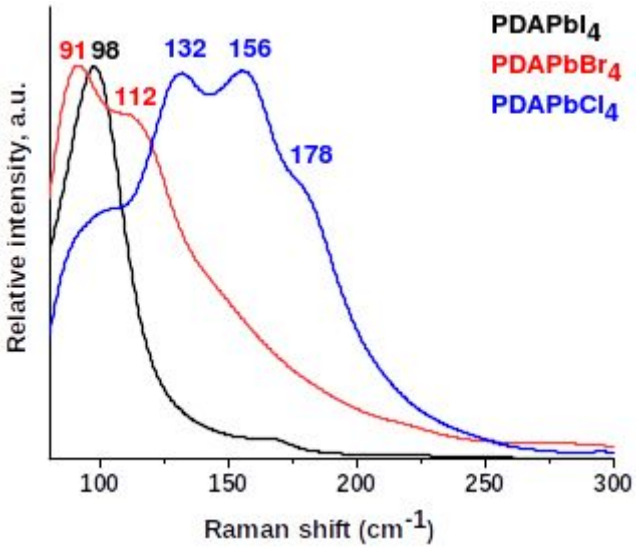

Figure 2. Raman spectra of lattice phonons in $PDAPbI_4$, $PDAPbBr_4$, and $PDAPbCl_4$.

Figure 2 shows that the breathing modes of $PDAPbI_4$ are represented by a single intense peak at 98 cm^{-1}. Phonon spectra of the bromide and chloride compounds show two (91 cm^{-1} and 112 cm^{-1}) and four (98 cm^{-1}, 132 cm^{-1}, 156 cm^{-1}, and 178 cm^{-1}) peaks, respectively. Such a difference in the lattice phonon vibrational region can be explained based on the structure of the considered compounds. The inorganic framework of $PDAPbI_4$ consists of identical, side-by-side arranged chains of almost regular face-sharing PbI_6 octahedra, while the layered structures of $PDAPbBr_4$ and $PDAPbCl_4$ are formed by corner-sharing $PbBr_6$ and $PbCl_6$ octahedra of several types. The higher number of peaks in the spectrum of $PDAPbCl_4$ as compared to that in the spectrum of $PDAPbBr_4$ is attributed to the following. The $PbCl_6$ octahedra feature larger displacement of Pb cations from the octahedron centers

as compared to the $PbBr_6$ octahedra. Besides, the $PbCl_6$ octahedra are more tilted than the $PbBr_6$ octahedra.

The higher frequency vibrations (>200 cm^{-1}) are due to the PDA cations. At these frequencies the heavy lead and halogen ions remain almost stationary.

The broad-band components are noted in the high-frequency range [2800-3300] cm^{-1} (see Figure 3a). The peaks at ~2863 cm^{-1} and ~2929 cm^{-1} correspond to the symmetric and antisymmetric stretching vibrations in the PDA methylene groups [34,35].

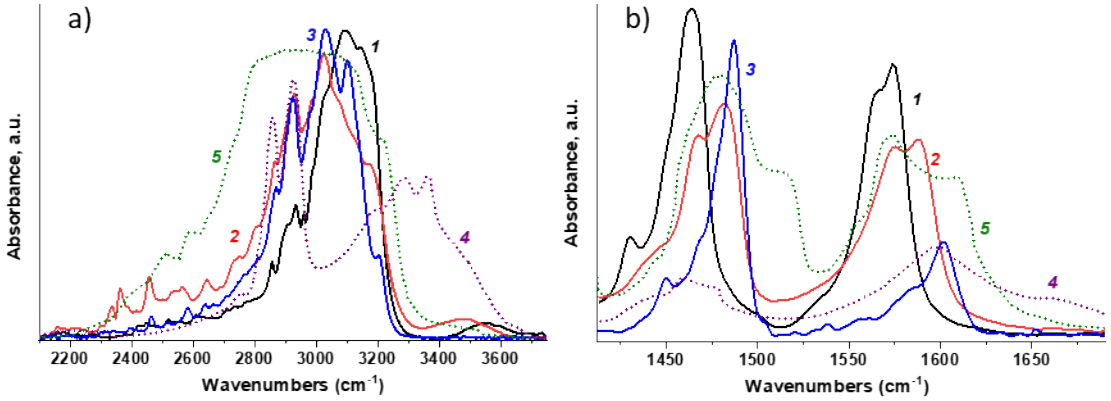

Figure 3. FTIR spectra of $PDAPbX_4$ in the ν(NH) (a) and δ(NH) (b) frequency regions: 1 – $PDAPbI_4$, 2 – $PDAPbBr_4$, 3 – $PDAPbCl_4$. The spectra of solid PDA (4) and PDA dihydrochloride (5) diluted in KBr pellets are presented for comparison [40].

The absorption band maxima appeared near 3093 cm^{-1}, 3025 cm^{-1}, and 3030 cm^{-1} for the iodide, bromide, and chloride compounds, respectively, can be assigned to the N–H stretching vibrations (see spectra 1-3). Due to the hydrogen bonding, these bands for salts of primary aliphatic amines are downshifted by ~250-300 cm^{-1} as compared to those for primary aliphatic amines in condensed phase or diluted in non-polar solvents [35,41,42]. The H-bonding effect on the band shape and band position can be clearly seen for PDA salt (spectrum 5) and PDA (spectrum 4), both diluted in potassium bromide [40]. In general, the greater the band downshift, the stronger the H-bonding. This results in wider absorption bands featuring more types of H-bonds in a system. It is known that for molecular complexes of ammonia or amines with hydrogen halides in a gas phase or in cryogenic matrices, the

energy required for dissociation of HX increases in the series I – Br – Cl – F [36-39]. Thus, the gradual weakening of the H–X bond promotes the formation such complexes.

In cryogenic matrices and in a gas phase, the halogen-involving vibrations of N···H···X and H–X types were detected for NH_3···HX complexes [36,43]. Such vibrations were not detected even for $PDAPbCl_4$ that is apparently due to the large number of halogen atoms weakening the intermolecular interactions.

Downshifts of ν(NH) are about the same for the bromide and chloride perovskites and greatly exceed that for the iodide compound. This may indicate a stronger interaction of nitrogen with protons of -NH_3^+ groups surrounded by halogens of the PbX_6 octahedra in $PDAPbBr_4$ and $PDAPbCl_4$ as compared to $PDAPbI_4$. It should be noted that the absorption range of N–H fragments involved in the formation of N–H···X-type bonds in $PDAPbBr_4$ is wider than that in $PDAPbCl_4$ and $PDAPbI_4$.

A thorough examination of the structures obtained from crystallographic data (Figure 1) allowed us to determine the nearest halogen environment for the nitrogen atoms in each sample. As a result, it was determined that in the structures of $PDAPbI_4$ and $PDAPbCl_4$ nitrogen atoms in -NH_3^+ groups are arranged uniformly throughout the structure, while for $PDAPbBr_4$ there are two slightly different configurations of the arrangement of -NH_3^+ groups in cavities formed by $PbBr_6$ octahedra.

Following the classification of the hydrogen bond by strength depending on the N-H distance and the relative Δν(NH) shift [44], the binding of the PDA ammonium groups with halogen atoms of the inorganic framework should be considered weak for all the perovskites. The analysis of structural data confirmed the conclusions about the strength and diversity of interactions of the N–H···X type in the studied perovskite materials made from spectroscopic data (Figure 3a).

The spectral manifestation of the H-bond can also be traced in the N–H deformation vibration range [35,45]. H-bonding shifts the N–H deformation band frequency to higher values.

In FTIR spectra, the most prominent features below 1600 cm^{-1} are complex absorption bands (see Figure 3b). The band at ~1622 cm^{-1} attributed to the alkyl-diamine NH_2 scissoring mode (spectrum *4*) is absent in the spectra of PDA salt (spectrum *5*) and PDA halide perovskites (spectra *1-3*) that confirms the high affinity of nitrogen in -NH_3^+ to the proton. In the range [1420-1500] cm^{-1}, the C–H

bending vibrations contribute to the complex band shape at ~1440-1450 cm^{-1}, as demonstrated by Raman and FTIR spectra in Figures S2 and S3. The peaks with maxima at 1450-1500 cm^{-1} and 1550-1625 cm^{-1} are related to the symmetric and antisymmetric bending vibrations in $-NH_3^+$ group, respectively [35,41,46]. The $\delta_s(NH)$ and $\delta_{asym}(NH)$ frequencies are as follows (see Figure 3b and Table S2). For $PDAPbI_4$: 1464 cm^{-1} (the shoulder at 1450 cm^{-1}) and 1574 cm^{-1} (the shoulder at 1565 cm^{-1}). For $PDAPbBr_4$: doublet with maxima at 1483 cm^{-1} and 1467 cm^{-1} and doublet with maxima at 1587 cm^{-1} and 1575 cm^{-1}. For $PDAPbCl_4$: 1487 cm^{-1} (shoulder at 1469 cm^{-1}) and 1602 cm^{-1} (shoulder at 1585 cm^{-1}). Obviously, with decreasing halogen size, a shift of both bands towards higher frequencies is observed. This result also confirms the strengthening of hydrogen bond N–H···X in the same halogen sequence [45].

Predominantly one narrow band in the iodide perovskite spectrum indicates a weak and uniform halogen environment of the $-NH_3^+$ groups in the inorganic matrix, and for bromide perovskite the presence of doublets for $\delta_s(NH)$ and $\delta_{asym}(NH)$ bands indicates the coexistence of two types of $-NH_3^+$ groups in the perovskite structure (Figure 3b). It should also be noted that spectra of all the perovskites reveal a band below 2000 cm^{-1} (see Figure S4) attributed to a combination of the C-C-N torsional vibration and the antisymmetric deformation vibration of $-NH_3^+$ groups (1550-1625 cm^{-1}) [35,42]. The presence of this spectral feature may indicate the lack of threefold symmetry of the pentadiamine cations [42].

The effect of H-bond on the primary amines spectra is the most clearly manifested in the range [700-1000] cm^{-1} where the broad absorption of weak-to-medium intensity alters in shape and position depending on the number of H-bonds present (compare spectra *1-4* with spectrum *5* in Figure S5). This range is mainly due to combination bands involving the H–N–H twisting (τ) and rocking (ρ) vibrations (see Table S2). Unfortunately, vibrations associated with the C–C–N angles and C–N bonds which are active in this spectral range as well complicate understanding of the H-bonding picture.

Thus, as far as the perovskite crystal structures is concerned the data obtained by IR spectroscopy confirm and complement the data obtained by XRD analysis. While XRD method is well-suited for studies of the inorganic subsystem of the perovskite crystal lattices, IR spectroscopy

allow us to describe interactions between their inorganic and organic subsystems. It was demonstrated that all the hydrogen atoms of the $-NH_3^+$ groups participate in the formation of N-H···X bonds. This is evidenced by the fact that in the IR spectra all the N-H vibrations are perturbed by H-bonding. No bands belonging to free N-H vibrations were observed.

3.3. Refinement of the $PDAPbBr_4$ perovskite crystal structure

In contrast to $PDAPbCl_4$ and $PDAPbI_4$, the structure of $PDAPbBr_4$ was poorly resolved and demonstrated duplicated atoms. In order to refine it a combinatorics approach was employed. First, out of the eight PDA chains present in the original unit cell of $PDAPbBr_4$ four distinct conformations meaningful from a chemical viewpoint and each containing four such chains were identified. This manipulation let us to get rid of duplicated C, N, and H atoms. Further analysis of the symmetry of the four PDA chain conformations revealed that only two of them are unique. Then, using combinatorics approach again, sixteen out of the thirty two bromine anions present in the original perovskite unit cell were chosen. This resulted in sixteen (organic chains conformation # 1) and seven hundred thirty six (organic chains conformation # 2) perovskite structures of non-trivial spatial symmetry i.e. belonging to a space group other than P1. The generated structures feature either triclinic (Space group P-1) or monoclinic (Space groups $P2_1$, Pc, $P2_1/c$) syngony. In total, fourteen highest symmetry structures (space group $P2_1/c$) were found. Space groups of other perovskites structures are subgroups of the space group $P2_1/c$. We therefore concluded that an actual bromide perovskite has the space group symmetry $P2_1/c$, while other perovskites symmetries are simply artifacts of the employed combinatorics approach. The final step of the $PDAPbBr_4$ structure refinement was to choose a single $P2_1/c$ structure out of the fourteen available. This was done based on total energy computations. The lowest energy structure was assumed to be a true one.

3.4 Electronic structures of the $PDAPbX_4$ perovskites

Figure 4 demonstrates electronic BS and DOS of the perovskites modeled using DFT. As can be seen from Figure 4a, the quasi 2D chloride perovskite (monoclinic; C2) is a semiconductor with the

direct VB→CB electronic transition occurring in-between the Γ and A k-points. The computed electronic bandgap equals 3.20 eV. This value matches well the bandgap of 3.036 eV recently reported for the same perovskite by W. Yang et al. [15]. However, the BS plot of $PDAPbCl_4$ presented in Figure 5b therein differs considerably from the one illustrated in Figure 4a of this work. Despite the similar structure (monoclinic; $P2_1/c$) the BS of $PDAPbCl_4$ features direct electronic transition at the Γ-point [15]. At present, we cannot offer any explanation for this discrepancy. What we found even more confusing is the reported high symmetry *k*-point path [15]. To the best of our knowledge, monoclinic syngony features no high symmetry *k*-points A1, R, and S [47].

Figure 4b shows that the quasi 2D bromide perovskite (monoclinic; $P2_1/c$) is a direct bandgap semiconductor as well. In contrast to the chloride, it features several energetically close VB→CB electronic transitions. They occur at the Γ, Y, and Y1 k-points. The computed electronic bandgap amounts to ~2.60 eV.

According to Figure 4c, the quasi 1D iodide perovskite (triclinic; P-1) is an indirect bandgap semiconductor. In this compound, electrons can be excited for the k-point of VB located in-between the Z and N k-points onto the Γ k-point of CB. For this perovskite, the calculations predict an electronic bandgap of 2.73 eV.

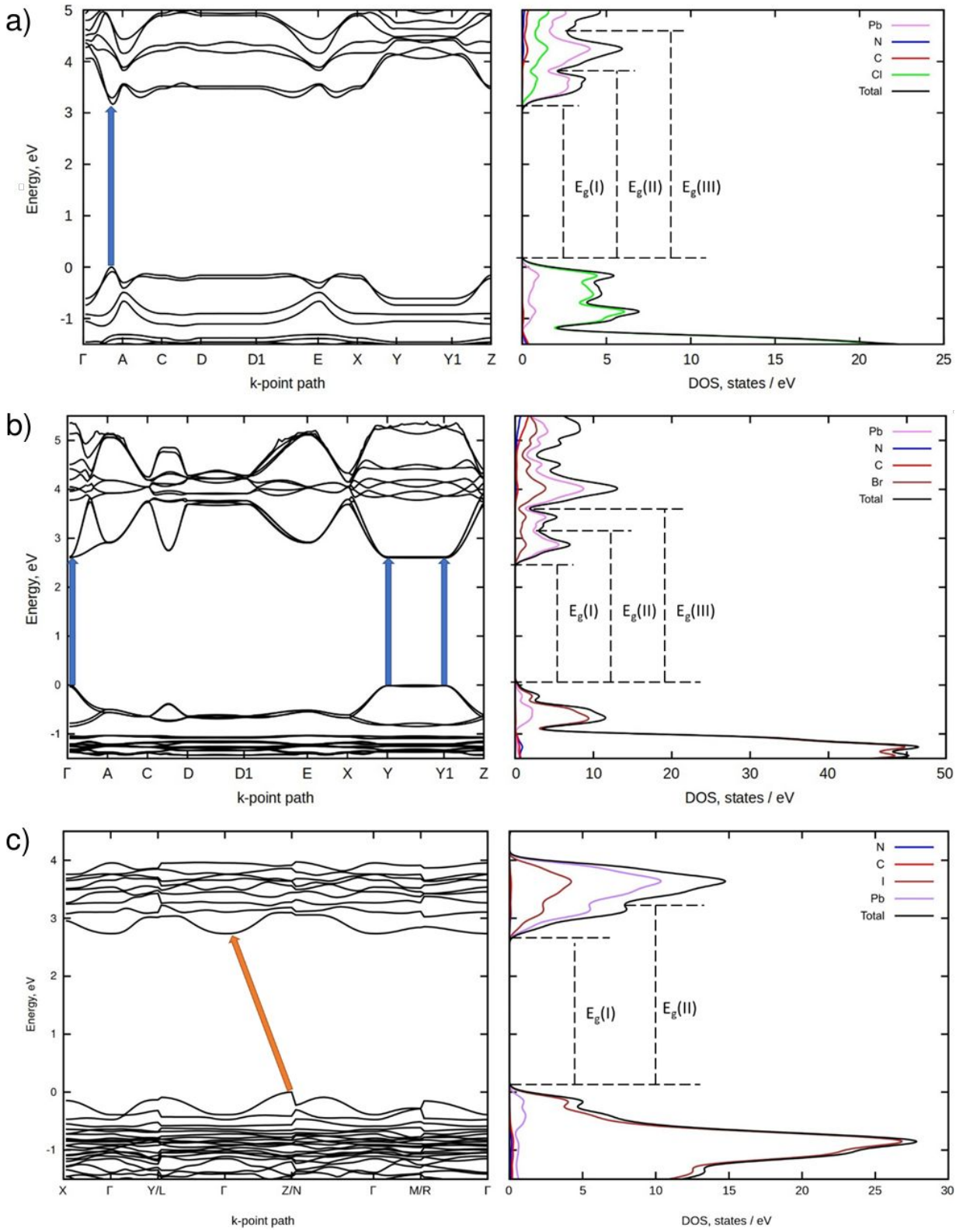

Figure 4. Electronic PBE BS (left) and DOS (right) of $PDAPbCl_4$ (a), $PDAPbBr_4$ (b), and $PDAPbI_4$ (c).

3.5 Optical properties of the $PDAPbX_4$ perovskites

Figure 5a shows diffuse reflectance spectra of the studied perovskites.

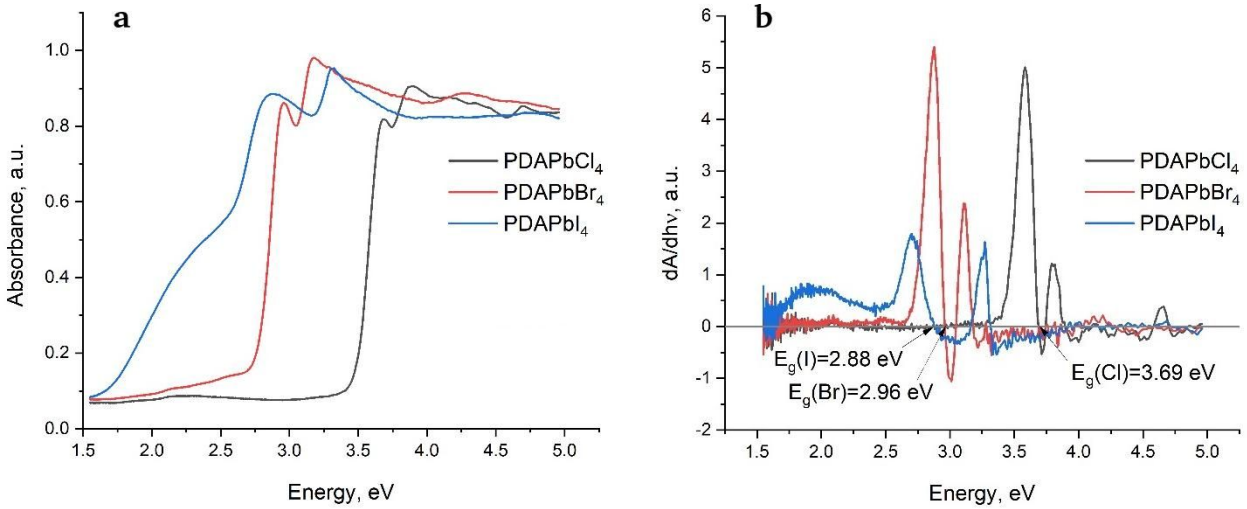

Figure 5. Diffuse reflectance spectra (a) and their derivative (b) for $PDAPbX_4$, (X = Cl, Br, I).

One can see that the chloride and bromide feature sharper edges of fundamental absorption as compared to the iodide that could be related to the larger number of defects in the latter. Optical bandgaps of the perovskites were determined as crosspoints of the diffuse reflectance spectra derivatives with X-axis (Figure 5b). They decrease in the sequence Cl-Br-I as follows E_g=3.69 eV (Cl), E_g=2.96 eV (Br), and E_g=2.88 eV (I) that is typical of metal halide perovskites. Figure 5b also shows that the second maxima of the derivatives are shifted towards higher energies. We have observed and explained such behavior in 1,6-hexamethylenediamine perovskites earlier [9].

As one can see from Table 2, there is a discrepancy between the theoretical (electronic) and experimental (optical) bandgaps of the perovskites. There are several reasons for it [48]. We shall remind the reader that the results of DFT calculations presented here formally correspond to 0 K as opposed to a finite temperature at which the diffuse reflectance spectra were recorded. It is known that many materials including semiconductors undergo thermal expansion often resulting in optical bandgaps which are larger than the predicted electronic ones. This could be one of the reasons why optical bandgaps listed in Table 2 are somewhat larger than their theoretical counterparts. Taking this into account we may conclude that the agreement between the experimental and theoretical bandgaps is rather satisfactory.

Table 2. Experimental (optical) and theoretical (electronic) bandgaps of $PDAPbX_4$ perovskites.

Compound	Experiment, eV	Theory, eV
$PDAPbCl_4$	3.69	3.20
$PDAPbBr_4$	2.96	2.60
$PDAPbI_4$	2.88	2.73

As speculated earlier, the second maxima in Figure 5b could be associated with VB→CB+1 electronic transitions [9]. In the case of chloride perovskite, the second maximum is observed experimentally at 3.89 eV, while the theoretical value predicted by DFT amounts to 3.62 eV. In the case of bromide perovskite, the second maximum is observed experimentally at 3.17 eV, whereas DFT predicts the value of 3.09 eV. Finally, in the case of iodide perovskite, the second maximum is observed experimentally at 3.32 eV, while DFT predicts 3.24. Thus, all the studied perovskites show very good agreement between the calculated and experimental energies of VB→CB+1 electronic transitions.

3.6 Luminescent properties of $PDAPbX_4$

Low-temperature luminescence spectra of the $PDAPbCl_4$ perovskite are demonstrated in Figure 6a.

In agreement with the data reported earlier [15], this hybrid perovskite is characterized by a single broad luminescence band in the region [450-700] nm (curves 1-2) with a maximum at ~550 nm which is most effectively excited by a radiation with wavelengths of 335 and 315 nm (curve 3). The sharp edge of the broadband luminescence at 340 nm agrees well with the determined optical bandgap of 3.69 eV (336 nm) meaning that the broadband luminescence of $PDAPbCl_4$ is due to interband excitation.

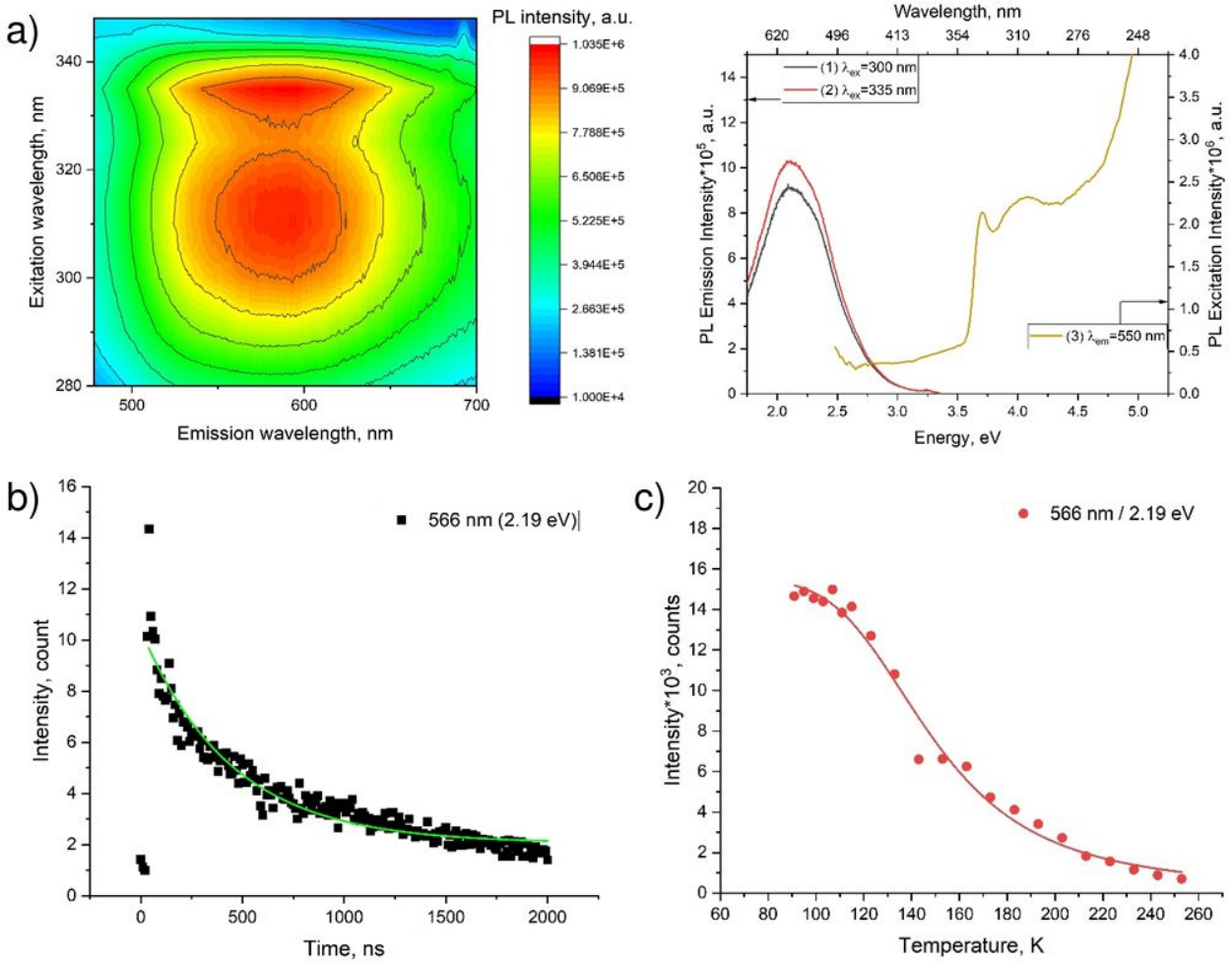

Figure 6. Luminescent properties of $PDAPbCl_4$: (a) Luminescence spectrum represented as 3D map (left) and spectral lines (right); (b) Low-temperature (78 K) decay kinetic of luminescence (line correspond to the fitting of the experimental data according to equation 4); (c) temperature dependence of the intensity of luminescence band (line correspond to the fitting of the experimental data according to equation 5).

Figure 6b shows the decay kinetics of characteristic luminescence band intensities of $PDAPbCl_4$. The kinetics of this process follows the exponential dependence:

$$I = I_0 e^{\frac{-t}{\tau}}, \qquad (4)$$

where τ is a characteristic life-time and I_0 is an amplitude.

Fitting the data for $PDAPbCl_4$ into equation (4) results in the broadband luminescence life-time of 458±77 ns.

As temperature increases the luminescence band intensity of the studied perovskites decreases due to the increase in efficiency of nonradiative recombination channels. Generally, the temperature dependence of luminescence intensity is well described by the Mott-Seitz equation [49,50]:

$$I(T) = \frac{I_0}{1 + Ae^{\frac{-E_a}{kT}}} \quad (5)$$

where I_0 - luminescence intensity at 0 K, E_a - activation energy, and A - dimensionless coefficient whose meaning depends on whether quenching is internal or external.

Figure 6c shows that the temperature quenching of broadband luminescence of $PDAPbCl_4$ with a maximum at 566 nm (2.19 eV) is well described by eq. 5 with E_a = ~67.8±6.5 meV.

Figure 7a illustrates the luminescence spectra and the spectra of luminescence excitation of $PDAPbBr_4$. Therein, one can see two components: the narrow band, short wavelength with the maximum at 414 nm and the wide band, long wavelength with the maximum at 530 nm. The peaks of both luminescence spectra coincide.

The edge of long wavelength luminescence excitation reaches 427 nm (2.90 eV) matching the perovskite optical bandgap (2.96 eV). Interestingly, the excitation spectra of both luminescence bands look alike. This might indicate that both channels of the radiative relaxation originate from the same excitation pathways due to the intrinsic light absorption.

Decay kinetics of characteristic luminescence band intensities of $PDAPbBr_4$ is demonstrated in Figure 7b. In this perovskite, the luminescence decay occurs much faster as compared to that in $PDAPbCl_4$. An application of eq. 4 to the experimental decay kinetics data results in characteristic life-times of 11±0.3 ns and 5±0.2 ns for the luminescence bands with the maxima at 530 nm and 414 nm, respectively. The latter value is very close to the duration of excitation laser pulse in Figure S6. This is the reason why an actual life-time of the narrow-band luminescence of $PDAPbBr_4$ could not be determined. Seemingly, it does not exceed 10 ns. Anyway, the difference in decay time for two luminescence bands infers that there exist two different channels of radiative relaxation corresponding to two observed luminescence bands.

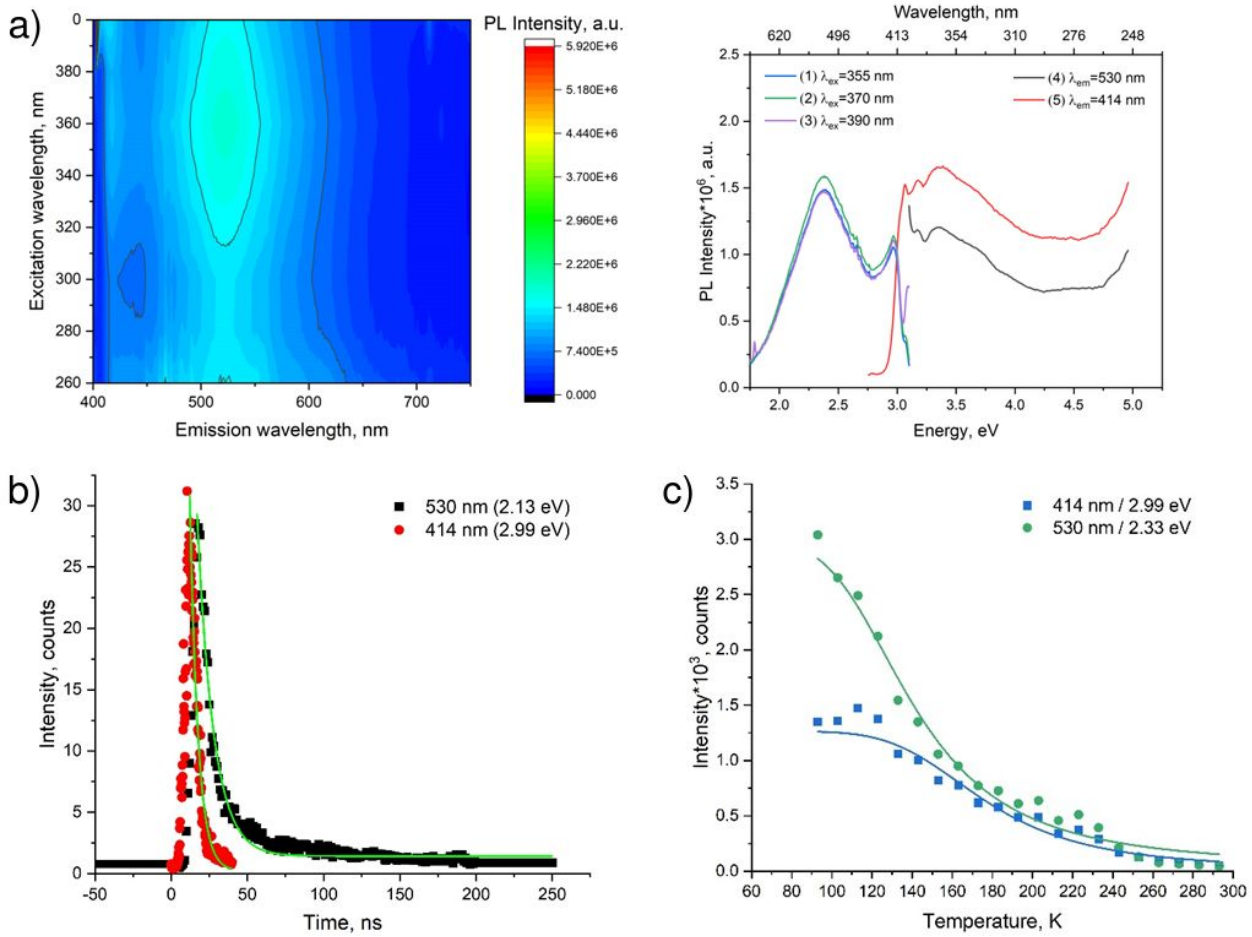

Figure 7. Luminescent properties of $PDAPbBr_4$: (a) Luminescence spectrum represented as 3D map (left) and spectral lines (right); (b) Low-temperature (78 K) decay kinetics of luminescence (lines correspond to the fitting of the experimental data according to equation 4); (c) temperature dependence of the intensity of luminescence bands (lines correspond to the fitting of the experimental data according to equation 5).

The quenching of both narrow- and broadband luminescence of $PDAPbBr_4$ (Figure 7c) is also well described by eq. 5. For the narrow-band luminescence with a maximum at 414 nm (2.99 eV) E_a = 100.4±9.4 meV, whereas for the broadband luminescence with a maximum at 530 nm (2.33 eV) E_a = 68.4±6.9 meV.

The luminescence spectra and the spectra of luminescence excitation of $PDAPbI_4$ are showed in Figure 8a. Therein, one can see two overlapping luminescence bands: the short wavelength in the range [575-725] nm and the long wavelength in the range [650-850] nm. The long wavelength luminescence excitation spectrum reaches 430 nm (2.88 eV) that corresponds to the interband

excitation of this perovskite. The luminescence excitation spectrum is complex and consists of several bands. Most efficiently the luminescence is excited by a radiation with the wavelengths of 240 nm, 330 nm, and 410 nm.

Figure 8b shows kinetics of decay of the short and long wavelength luminescence of $PDAPbI_4$. Having approximated the data according to eq. 4, we obtain characteristic life-times of 11.4±0.52 ns and 12.11±0.8 ns for the luminescence bands with the maxima at 650 nm and 800 nm, respectively. Such similar lifetimes of the luminescence might indicate a similarity in relaxation mechanisms for both luminescence bands.

The quenching of both closely spaced luminescence bands (with the maxima at 650 nm and 800 nm) in $PDAPbI_4$ (Figure 8c) occurs with activation energies on the order of 49 meV (49.4±1.9 meV and 49.1±1.8 meV, respectively).

Table 3 shows how luminescent properties of $PDAPbX_4$, (X = Cl, Br, I) depend on the type of halogen atom. According to it, the bromide perovskite features two luminescence channels: free excitons (FE) and self-trapped excitons (STE). Noteworthy, the narrow-band FE-luminescence is more stable than the broad-band STE-luminescence. The other compounds demonstrate just one radiative recombination channel which is STE. The two luminescence bands in the iodide perovskite case correspond to two types of STE localization states.

Table 3. Luminescence band maximum at 83 K (nm/eV), characteristic lifetimes (ns), and luminescence quenching activation energy E_a (meV) of the luminescence bands of $PDAPbX_4$ (X = Cl, Br, I) perovskites.

Compound	L. max at 83 K	lifetime	L. quenching E_a
$PDAPbCl_4$	566/2.19	458±77	67.8±6.5
$PDAPbBr_4$	414/2.99	≤5	100.4±9.4
$PDAPbBr_4$	530/2.33	11.0±0.30	68.4±6.9
$PDAPbI_4$	650/1.91	11.4±0.52	49.4±1.9
$PDAPbI_4$	800/1.55	12.11±0.8	49.1±1.8

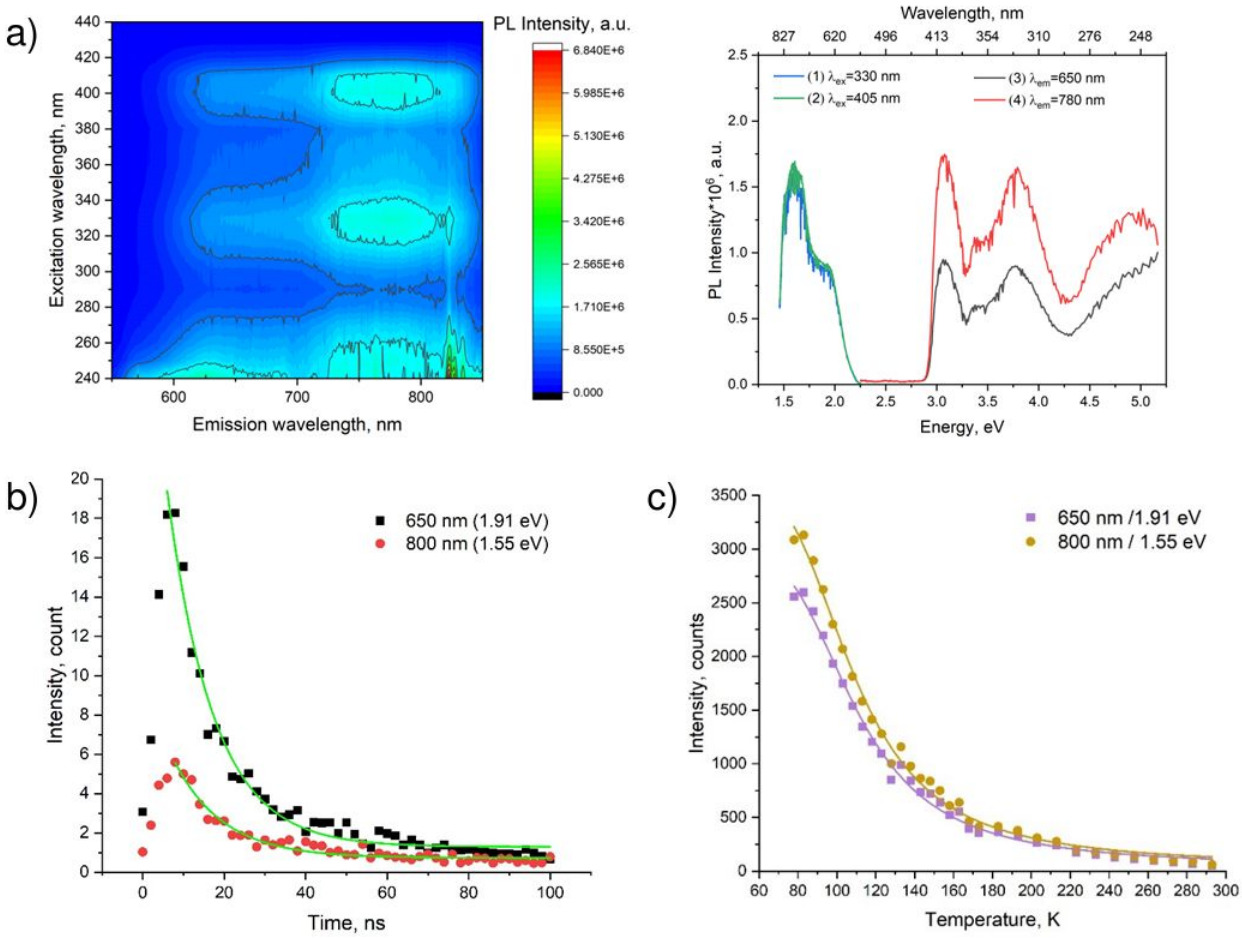

Figure 8. Luminescent properties of $PDAPbI_4$: (a) Luminescence spectrum represented as 3D map (left) and spectral lines (right); (b) Low-temperature (78 K) decay kinetics of luminescence (lines correspond to the fitting of the experimental data according to equation 4); (c) temperature dependence of the intensity of luminescence bands (lines correspond to the fitting of the experimental data according to equation 5).

4. Discussion

The considered $PDAPbX_4$, (X=Cl, Br, I) perovskites differ from each other only in the type of constituting halogen atom. This lets us to uncover how halogen atoms affect the perovskite crystal structures and, as a result, their optoelectronic properties.

There are two ways halogen atoms influence the formation of crystal structures of low-dimensional perovskites. The first one is a dimensionality factor. Indeed, the halogen atoms differ in size which increases in the sequence Cl-Br-I. The second is a strength with which halogen atom interacts with the organic cation and lead atom. This strength depends on halogen atom

electronegativity which decreases in the same sequence. The cumulative effect of both leads to a formation of wide variety of hybrid perovskites of different anionic compositions.

The inorganic $PbCl_6$ octahedra network within the chloride perovskite structure undergoes both disorder and distortion. The former manifests itself in significant $PbCl_6$ octahedra tilts with respect to each other, while the latter results in a slight asymmetry of the octahedra themselves. Thus, in the case of chloride perovskite optimal positions of the $PbCl_6$ octahedra with respect to the PDA amino groups is achieved via tilting of the former. In contrast, in the case of bromide perovskite the same goal is achieved through the $PbBr_6$ octahedra distortion. Yet another scenario is realized in the iodide perovskite case. As a matter of fact, optimal interactions between the organic and inorganc subsystems in this perovskite are fulfilled when the PbI_6 octahedra are connected with each other through common faces and edges forming a quasi 1D structure.

Electrostatic interactions between cations and anions of a perovskite play an important role in its formation. In the context of this study, they arise between lead, halogen, and PDA ions. An optimal arrangement of the PDA protonated amino groups within the perovskite crystals is such that their three hydrogens point toward the nearest halogens thereby forming H-bonds. This is confirmed by the IR spectra lacking bands due to non-interacting N-H bonds. Thus, an optimal PDA orientation with respect to the PbX_6 octahedra implies the formation of three H-bonds between the protonated amino groups and halogens.

We would like to emphasize that, here, H-bonds play rather minor role as they are much weaker than electrostatic interactions occurring between the perovskite ions. Nevertheless, all the three considered perovskites feature the H-bond formation that leads to a total energy lowering.

In fact, the recorded XRD data revealed that PDA^+ in $PDAPbBr_4$ perovskite have two distinct conformations as showed in Figure 9. The major difference between them is the orientation of one of the amino groups with respect to the neighboring $PbBr_6$ octahedra (compare positions of the atoms N2 and N2A in Figure 9). This can also be regarded as a manifestation of intention of a perovskite to form as many H-bonds N-H···X as possible thereby stabilizing its structure.

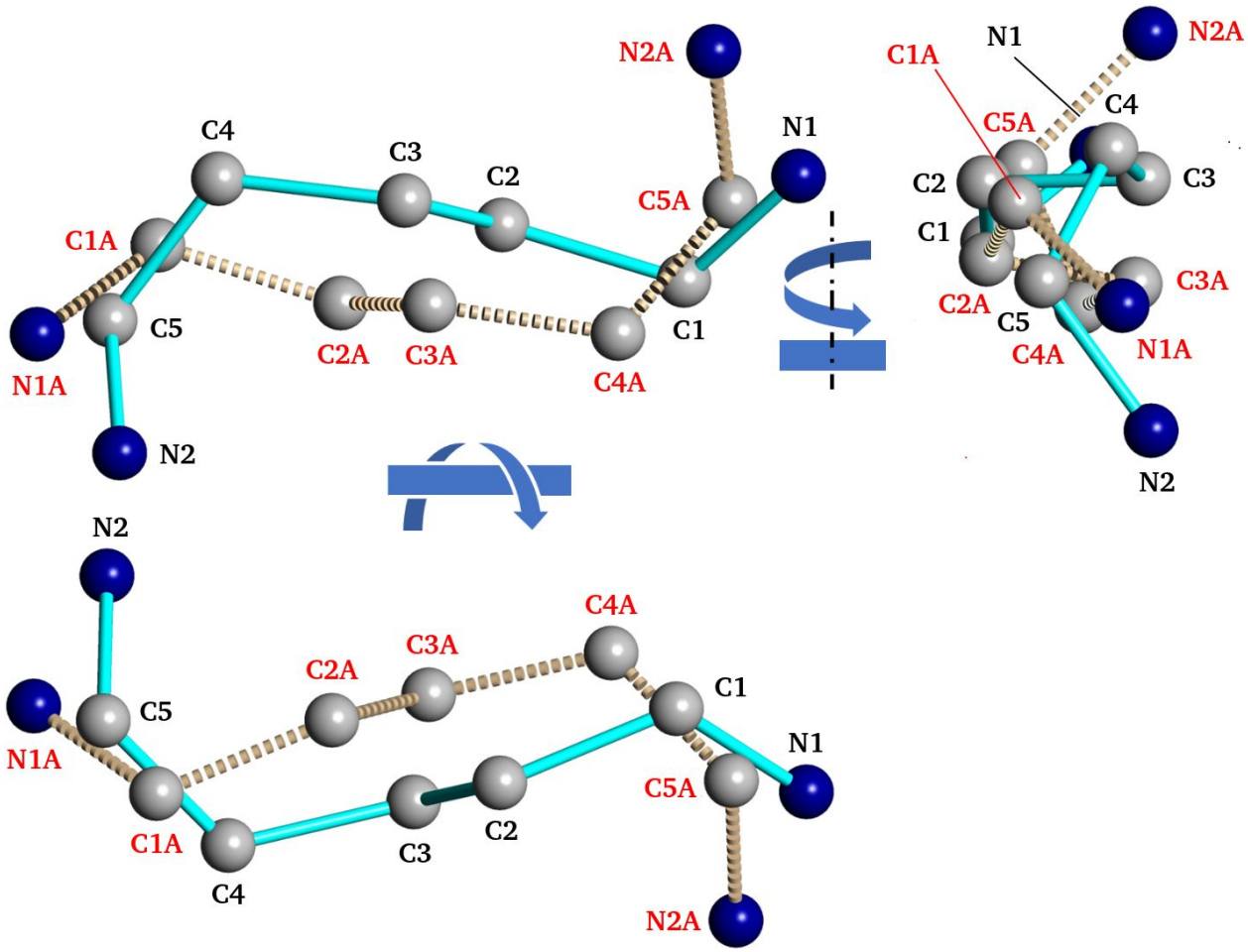

Figure 9. Two conformations of pentadiamine cation within the unit cell of $PDAPbBr_4$.

As indicated by excitation spectra and decay times of the luminescence, its excitation mechanism in all the three perovskites involves band to band transitions. However, the observed structure of the luminescence excitation spectra manifests the different character of these transitions between different electronic band states. In the case of luminescence spectra of $PDAPbCl_4$ perovskite, the wavelength of 335 nm (3.70 eV) corresponds to the electron transition from the top of VB to the bottom of CB (denoted as Eg(I) in Figure 4). This transition matches well the experimentally determined optical bandgap of 3.69 eV. In contrast, the wavelength of 315 nm (3.93 eV) seems to correspond to VB → CB+1 electron transition (denoted as Eg(II) in Figure 4). This transition is observed by diffuse reflectance spectroscopy and corresponds to the second maximum of the absorption derivative reported in Section 3.4 (3.89 eV). These features of the electronic structure and optical behavior of the synthesized materials can be attributed to the quantum size confinement effect

that, in turn, creates strong optical and electronic anisotropy in crystals reflecting the strong crystal structure anisotropy typical of low dimensional perovskites and their derivatives.

The obtained luminescence spectra can be represented as dots on the CIE 1931 color space shown in Figure 10. As can be seen, $PDAPbBr_4$ is a material with a great white light emission potential.

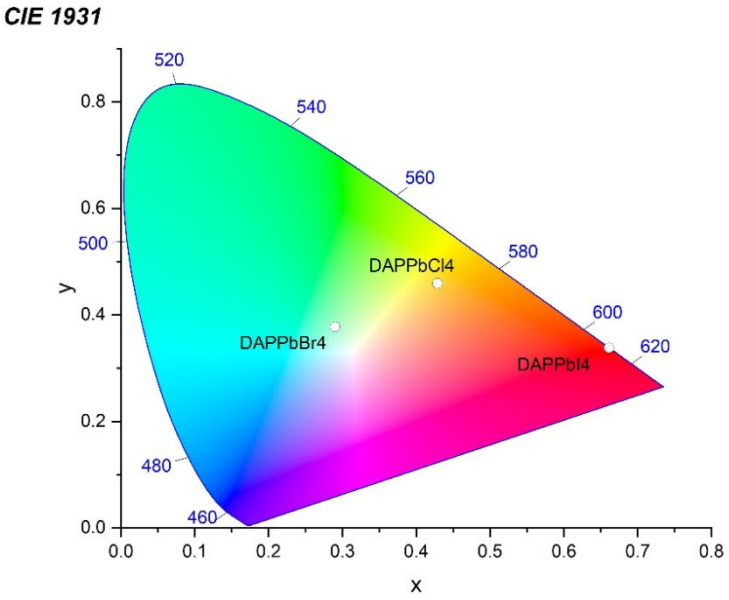

Figure 10. CIE 1931 color space with the marked positions of the luminescence spectra of various hybrid perovskites $PDAPbX_4$ (X = Cl, Br, I). For the chloride perovskite, the luminescence excitation wavelength is given in parentheses.

5. Conclusions

In the present work, the synthesis, structure, optoelectronic, and luminescence properties of $PDAPbX_4$ (X = Cl, Br, I) hybrid perovskites are reported. In contrast to their quasi 1D iodide analog, the chloride and bromide haloplumbates possess quasi 2D perovskite-like structure.

The role of a size of halogen anion and the strength of its interaction with the PDA and lead cations is elucidated. It is shown that the halogen anions determine the degree of the PbX_6 octahedra distortion and overall disorder of the perovskite crystal lattices. The PbX_6 octahedra distortion may result in asymmetry of Pb-X bond lengths and/or in the displacement of lead cation from its ideal position within the octahedron. An overall perovskite crystal lattice disorder is achieved through the

PbX_6 octahedra tilting. In extreme case ($PDAPbI_4$), the PbX_6 octahedra tilting may lead to their specific connection pattern in which the neighboring PbX_6 octahedra share their edges and faces as opposed to the corner-sharing pattern observed in $PDAPbCl_4$ and $PDAPbBr_4$. The orientation of terminal protonated amino groups changes as well subject to a type of halogen atom. An optimal perovskite structure explores all of the above-mentioned possibilities. One of the manifestations of such structure is a formation of as many H-bonds N-H···X as possible.

Author contributions

1. Conceptualization: D.S. Shtarev, A.V. Emeline
2. Data Curation: M.I. Balanov, D.A. Zharovov, K.M. Bulanin
3. Formal Analysis: D.S. Shtarev, A.V. Gerasimenko, R. Kevorkyants, D.A. Chaplygina, K.M. Bulanin, D.V. Pankin, A.V. Rudakova
4. Funding Acquisition: D.S. Shtarev
5. Investigation: R. Kevorkyants, M.I. Balanov, A. Ju. Major, A.V. Gerasimenko, D.A. Zharovov, K.M. Bulanin
6. Methodology: D.S. Shtarev, R. Kevorkyants
7. Project Administration: N.I. Selivanov
8. Resources: D.S. Shtarev, A.Ju. Major, A.V. Gerasimenko, A.V. Emeline
9. Software: R, Kevorkyants, D.V. Pankin
10. Supervision: D.S. Shtarev
11. Validation: A.V. Emeline, N.I. Selivanov
12. Visualization: R. Kevorkyants, D.S. Shtarev
13. Writing – Original Draft: D.S. Shtarev, R. Kevorkyants
14. Writing – Review & Editing: D.S. Shtarev, R, Kevorkyants, K.M. Bulanin, A.V. Rudakova, A.V. Emeline

Conflict of interest

There are no conflicts to declare

Acknowledgments

The study has been supported by the FEFU Foundation, project No. 22-03-03 004 and Ministry of Science and Higher Education of the Russian Federation (Mega Grant no. 075-15-2022-1112). Luminescence spectral studies were performed in the laboratory "Photoactive nanocomposite materials" supported by Saint-Petersburg University (project ID: 94030186). The authors are very grateful to the staff of the Joint Center for Collective Use of FEFU, as well as to the NanoPhotonics Resource Center, Centre for Optical and Laser Materials Research, Computing Center of the Research Park at the Saint Petersburg State University for their valuable assistance.

References

1. M.A. Green, E.D. Dunlop. J. Hohl-Ebinger, M. Yoshita, N. Kopidakis, A.W.Y. Ho-Baillie, Solar cell efficiency tables (Version 55), Prog. Photovolt. Res. Appl. 28 (2020) 3-15, https://doi.org/ 10.1002/pip.3228
2. H. Cho, S. Jeong, M. Park, Y. Kim, C. Wolf, C. Lee, J.H. Heo, A. Sadhanala, N. Myoung, S. Yoo, S. Im, R. Friend, T. Lee, Overcoming the electroluminescence efficiency limitations of perovskite light-emitting diodes, Science 350 (2015) 1222−1225, https://doi.org/10.1126/ science.aad1818
3. N. Wang, L. Cheng, R. Ge, S. Zhang, Y. Miao, W. Zou, C. Yi, Y. Sun, Y. Cao, R. Yang, Y. Wei, Q. Guo, Y. Ke, M. Yu, Y. Jin, Y. Liu, Q. Ding, D. Di, L. Yang, G. Xing, H. Tian, C. Jin, F. Gao, R.H. Friend, J. Wang, W. Huang, Perovskite light-emitting diodes based on solution-processed self-organized multiple quantum wells, Nat. Photonics 10 (2016) 699−704, https://doi.org/ 10.1038/nphoton.2016.185
4. Z. Xiao, R.A. Kerner, L. Zhao, N.L. Tran, K.M. Lee, T.-W. Koh, G.D. Scholes, B.P. Rand, Efficient perovskite light-emitting diodes featuring nanometre-sized crystallites, Nat. Photonics 11 (2017) 108−115, https://doi.org/10.1038/nphoton.2016.269

5. X. Li, Y. Wu, S. Zhang, B. Cai, Y. Gu, J. Song, H. Zeng, $CsPbX_3$ quantum dots for lighting and displays: Room-temperature synthesis, photoluminescence superiorities, underlying origins and white light-emitting diodes, Adv. Funct. Mater. 26 (2016) 2435–2445, https://doi.org/10.1002/adfm.201600109

6. H. Zhu, Y. Fu, F. Meng, X. Wu, Z. Gong, Q. Ding, M.V. Gustafsson, M.T. Trinh, S. Jin, X.Y. Zhu, Lead halide perovskite nanowire lasers with low lasing thresholds and high quality factors, Nat. Mater. 14 (2015) 636-642, https://doi.org/10.1038/nmat4271

7. S.K. Abdel-Aal, G. Kocher-Oberlehner, A. Ionov & R.N. Mozhchil, Effect of organic chain length on structure, electronic composition, lattice potential energy, and optical properties of 2D hybrid perovskites $[(NH_3)(CH_2)_n(NH_3)]CuCl_4$, n=2–9, Appl. Phys. A 123 (2017) 531, https://doi.org/10.1007/s00339-017-1150-8

8. J.A. McNulty, P. Lightfoot, Structural chemistry of layered lead halide perovskites containing single octahedral layers. Chemical crystallography and crystal engineering, 8 (2021) 485–513, https://doi.org/10.1107/S2052252521005418

9. M.I. Balanov, O.A. Brylev, V.V. Korochencev, R. Kevorkyants, A.V. Emeline, N.I. Selivanov, Y.V. Chizhov, A.V. Syuy, D.S. Shtarev. Crystal structure and electronic properties of low-dimensional hexamethylenediaminium lead halide perovskites, Dalton Trans. 52 (2023) 6388-6397, https://doi.org/10.1039/D3DT00438D

10. L. Mao, P. Guo, M. Kepenekian, I. Spanopoulos, Y. He, C. Katan, J. Even, R. Schaller, R. Seshadri, C.C. Stoumpos, M.G. Kanatzidis, Organic cation alloying on intralayer A and interlayer A' sites in 2D hybrid Dion-Jacobson lead bromide perovskites $(A')(A)Pb_2Br_7$, J. Am. Chem. Soc. 142 (2020) 8342–8351, https://doi.org/10.1021/jacs.0c01625

11. E.J. Crace, A.C. Su, H.I. Karunadasa, Reliably obtaining white light from layered halide perovskites at room temperature, Chem. Sci. 13 (2022) 9973–9979, https://doi.org/10.1039/d2sc02381d

12. S. Kahmann, D. Meggiolaro, L. Gregori, E.K. Tekelenburg, M. Pitaro, S.D. Stranks, F. De Angelis, M.A. Loi, The origin of broad emission in ⟨100⟩ two-dimensional perovskites:

Extrinsic vs. intrinsic processes, ACS Energy Lett. 7 (2022) 4232−4241, https://doi.org/10.1021/acsenergylett.2c02123

13. C. Deng, G. Zhou, D. Chen, J. Zhao, Y. Wang, Q. Liu, Broadband photoluminescence in 2D organic−inorganic hybrid perovskites: $(C_7H_{18}N_2)PbBr_4$ and $(C_9H_{22}N_2)PbBr_4$, J. Phys. Chem. Lett. 11 (2020) 2934−2940, https://dx.doi.org/10.1021/acs.jpclett.0c00578
14. D.G. Billing, A. Lemmerer, Bis(pentane-1,5-diammonium) decaiodotriplumbate(II), Acta Cryst. C60 (2004) m224-m226, https://doi.org/10.1107/S0108270104007553
15. W. Yang, X. Xiao, H. He, G. Tong, J. Hu, X. Xiao, J. Chen, M. Li, Y. He, Intermolecular hydrogen-bonding correlated structure distortion and broadband white-light emission in 5-ammonium valeric acid templated lead chloride perovskites, Cryst. Growth Des. 21 (2021) 5731−5739, https://doi.org/10.1021/acs.cgd.1c00566
16. Bruker. APEX 2. BrukerAXS Inc., Madison, Wisconsin, USA, 2008.
17. G. Kresse and D. Joubert, From ultrasoft pseudopotentials to the projector augmented-wave method, Phys. Rev. B 59 (1999) 1758-1775, https://doi.org/10.1103/PhysRevB.59.1758
18. J.P. Perdew, K. Burke, M. Ernzerhof, Generalized gradient approximation made simple, Phys. Rev. Lett. 77 (1996) 3865-3868, https://doi.org/10.1103/PhysRevLett.77.3865
19. J.P. Perdew, K. Burke, M. Ernzerhof, Erratum: Generalized gradient approximation made simple, Phys. Rev. Lett. 77 (1996) 3865-3868. Phys. Rev. Lett. 78 (1997) 1396 (erratum), https://doi.org/10.1103/PhysRevLett.78.1396
20. G. Kresse and J. Hafner, Ab initio molecular dynamics for liquid metals, Phys. Rev. B 47 (1993) 558-561, https://doi.org/10.1103/PhysRevB.47.558
21. G. Kresse and J. Hafner, Ab initio molecular-dynamics simulation of the liquid-metal-amorphous-semiconductor transition in germanium, Phys. Rev. B 49 (1994) 14251-14269, https://doi.org/10.1103/PhysRevB.49.14251
22. G. Kresse and J. Furthmüller, Efficiency of ab-initio total energy calculations for metals and semiconductors using a plane-wave basis set, Comput. Mat. Sci. 6 (1996) 15-50, https://doi.org/ 10.1016/0927-0256(96)00008-0

23. G. Kresse and J. Furthmüller, Efficient iterative schemes for ab initio total-energy calculations using a plane-wave basis set, Phys. Rev. B 54 (1996) 11169-11186, https://doi.org/10.1103/PhysRevB.54.11169

24. H.J. Monkhorst and J.D. Pack, Special points for Brillouin-zone integrations, Phys. Rev. B 13 (1976) 5188-5192, https:// doi.org/10.1103/PhysRevB.13.5188

25. T. Williams, C. Kelley, E.A. Merritt, C. Bersch, H.-B. Bröker, J. Campbell, R. Cunningham, D. Denholm, G. Elber, R. Fearick, C. Grammes, L. Hart, L. Hecking, P. Juhász, T. Koenig, D. Kotz, E. Kubaitis, R. Lang, T. Lecomte, A. Lehmann, J. Lodewyck, A. Mai, B. Märkisch, P. Mikulík, D. Sebald, C. Steger, S. Takeno, T. Tkacik, J. van der Woude, J.R. van Zandt, A. Woo, J. Zellner, Gnuplot 5.2: An interactive plotting program, 2018.

26. K. Momma, F.J. Izumi, VESTA: A three-dimensional visualization system for electronic and structural analysis, J. Appl. Crystallogr. 41 (2008) 653-658, https://doi.org/10.1107/S0021889808012016

27. S.J. Clark, M.D. Segall, C.J. Pickard, P.J. Hasnip, M.J. Probert, K. Refson, M.C. Payne, First principles methods using CASTEP, Z. Kristallogr. Cryst. Mater. 220 (2005) 567-570 (2005), https://doi.org/10.1524/zkri.220.5.567.65075

28. K. Refson, P.R. Tulip, and S.J. Clark, Variational density functional perturbation theory for dielectrics and lattice dynamics, Phys. Rev. B 73 (2006) 155114, https://doi.org/10.1103/PhysRevB.73.155114

29. J. Aarons, A new CASTEP and ONETEP geometry optimiser, http://www.hector.ac.uk/cse/distributedcse/reports/castep-geom/castep-geom/HTML/dCSE_project.html

30. X. Gonze and C. Lee, Dynamical matrices, Born effective charges, dielectric permittivity tensors, and interatomic force constants from density-functional perturbation theory, Phys. Rev. B 55 (1997) 10355, https://doi.org/10.1103/PhysRevB.55.10355

31. G.M. Sheldrick, SHELXT – Integrated space-group and crystal-structure determination, Acta Cryst. A71 (2015) 3–8, http://doi:10.1107/S2053273314026370

32. D. Cortecchia, J. Yin, A. Petrozza, C. Soci, White light emission in low-dimensional perovskites. J. Mater. Chem. C 7 (2019) 4956-4969, http://doi: 10.1039/c9tc01036j

33. C.C. Stoumpos, M.G. Kanatzidis, The renaissance of halide perovskites and their evolution as emerging semiconductors, Acc. Chem. Res. 48 (2015) 2791−2802, https://doi.org/10.1021/acs.accounts.5b00229

34. D.W. Mayo, F.A. Miller, R.W. Hannah, Course notes on the interpretation of infrared and Raman spectra, John Wiley & Sons Inc., 2004.

35. G. Socrates, Infrared and Raman characteristic group frequencies: Tables and charts, John Wiley & Sons Inc., 2004.

36. A.C. Legon, The nature of ammonium and methylammonium halides in the vapour phase: hydrogen bonding versus proton transfer, Chem. Soc. Rev. 22 (1993) 153-163, https://doi.org/10.1039/CS9932200153

37. A.J. Barnes and M.P. Wright, Strongly hydrogen-bonded molecular complexes studied by matrix isolation vibrational spectroscopy. Part 3.—Ammonia–hydrogen bromide and amine–hydrogen bromide complexes, J. Chem. Soc., Faraday Trans. 2, 82 (1986) 153-164, https://doi.org/10.1039/F29868200153

38. S.Md. Pratik, S. Chakraborty, S. Mandal, and A. Datta, Cooperativity in a new role: Stabilization of the ammonium salts in the solid state over their H-bonded complexes in the gas phase, J. Phys. Chem. C 119 (2015) 926–933, https://doi.org/10.1021/jp510479n

39. J.A. Snyder, R.A. Cazar, A.J. Jamka, and F.-M. Tao, Ab initio study of gas-phase proton transfer in ammonia−hydrogen halides and the influence of water molecules, J. Phys. Chem. A 103 (1999) 7719-7724, https://doi.org/10.1021/jp991918j

40. https://webbook.nist.gov/cgi/cbook.cgi?ID=C462942;https://webbook.nist.gov/cgi/cbook.cgi?ID=B6009315

41. M.E. Baldwin, The infrared spectra of some diamines and diamine salts, Spectrochim. Acta 18 (1962) 1455-1461, https://doi.org/10.1016/0371-1951(62)80006-X

42. A. Cabana, C. Sandordy, The infrared spectra of solid methylammonium halides, Spectrochim. Acta 18 (1962) 843-861, https://doi.org/10.1016/0371-1951(62)80089-7

43. L. Andrews, X. Wang, and Z. Mielke, Infrared spectrum of the $H_3N{-}HCl$ complex in solid Ne, Ne/Ar, Ar, and Kr. Matrix effects on a strong hydrogen-bonded complex, J. Phys. Chem. A 105 (2001) 6054-6064, https://doi.org/10.1021/jp010323x

44. T. Steiner, The hydrogen bond in the solid state, Angew. Chem. Int. Ed. 41 (2002) 48-76, https://doi.org/10.1002/1521-3773(20020104)41:1<48::AID-ANIE48>3.0.CO;2-U

45. K. Nakamoto, Infrared and Raman Spectra of Inorganic and Coordination compounds. 4th Ed., Wiley and Sons Inc., 1986.

46. J. Bellanato, Infra-red spectra of ethylenediamine dihydrochloride and other amine hydrochlorides in alkali halide disks, Spectrochim. Acta 16 (1960) 1344-1357, https://doi.org/10.1016/S0371-1951(60)80008-2

47. W. Setyawan, S. Curtarolo, High-throughput electronic band structure calculations: Challenges and tools, Comput. Mater. Sci. 49 (2010) 299-312, https://doi.org/10.1016/j.commatsci.2010.05.010

48. J. Wiktor, U. Rothlisberger, and A. Pasquarello, Predictive determination of band gaps of inorganic halide perovskites, J. Phys. Chem. Lett. 8 (2017) 5507-5512, https://doi.org/10.1021/acs.jpclett.7b02648

49. N.F. Mott and R.W. Gurney, in: Electronic Processes in Ionic Crystals, 2nd Ed., Oxford University Press, London, 1948.

50. F. Seitz, Speculations on the properties of the silver halide crystals, Rev. Modern Phys. 23 (1951) 328-352, https://doi.org/10.1103/RevModPhys.23.328